Graphene and cobalt phosphide nanowire composite as an anode material for high performance lithium-ion batteries

Jun Yang[1], Yu Zhang[2], Chencheng Sun[1], Hongzheng Liu[2], Laiquan Li[1], Weili Si[1], Wei Huang[1], Qingyu Yan[2] (✉), and Xiaochen Dong[1] (✉)

[1] Key Laboratory of Flexible Electronics (KLOFE) & Institute of Advanced Materials (IAM), Jiangsu National Synergetic Innovation Center for Advanced Materials (SICAM), Nanjing Tech University (NanjingTech), Nanjing 211816, China
[2] School of Materials Science and Engineering, Nanyang Technological University, Singapore 639798, Singapore

ABSTRACT

The synthesis of a composite of cobalt phosphide nanowires and reduced graphene oxide (denoted CoP/RGO) via a facile hydrothermal method combined with a subsequent annealing step is reported. The resulting composite presents large specific surface area and enhanced conductivity, which can effectively facilitate charge transport and accommodates variations in volume during the lithiation/de-lithiation processes. As a result, the CoP/RGO nanocomposite manifests a high reversible specific capacity of 960 mA·h·g^{-1} over 200 cycles at a current density of 0.2 A·g^{-1} (297 mA·h·g^{-1} over 10,000 cycles at a current density of 20 A·g^{-1}) and excellent rate capability (424 mA·h·g^{-1} at a current density of 10 A·g^{-1}).

1 Introduction

With the increasing demand for sustainable and renewable energy resources, great attention has been paid to developing high-performance electrochemical energy storage systems, such as batteries and super-capacitors [1, 2]. As one of the most promising power sources, rechargeable lithium-ion batteries have attracted a large amount of attention, with potential for application in portable electronics, hybrid electric vehicles, and electric vehicles. To this end, the development of novel electrode materials is one of the key tasks in developing next-generation lithium-ion batteries with high capacities, rapid charge–discharge rates, and long-term cyclabilities [3–5]. At present, various transition metal oxides have been intensively investigated as potential alternatives to graphite-based anode materials for lithium-ion batteries due to their

---

Address correspondence to Qingyu Yan, alexyan@ntu.edu.sg; Xiaochen Dong, iamxcdong@njtech.edu.cn

high theoretical capacities [6–10]. However, their low electrical conductivities lead to inferior charge–discharge rate capabilities. Thus, extensive research efforts are now being made to fabricate novel electrode materials.

Transition metal phosphides, such as Ni_2P [11, 12], FeP [13, 14], CoP [15, 16], Cu_3P [17], and MoP [18], are of interest for energy storage and electrochemical catalysis due to their relatively low charge–discharge potentials [19], metallic characteristics, and good thermal stabilities [20]. It has been found that the phosphide group possesses a lone pair of electrons in a 3p orbital and vacant 3d orbitals, which can enhance local charge density and accommodate surface charge states [21, 22]. There have been few reports regarding the lithium storage properties of transition metal phosphides. In particular, CoP is expected to be a promising anode material because of its high theoretical capacity (894 mA·h·g^{-1}) compared with that of commercial graphite (372 mA·h·g^{-1}). However, the use of CoP for lithium storage still remains unexplored. Graphene and graphene-integrated electrodes are also of interest in this field, because they can boost energy storage and conversion performance thanks to their unique physical and chemical properties [23].

Herein, we describe a two-step strategy to prepare a CoP nanowire/reduced graphene oxide (RGO) composite. First, the precursor $Co(CO_3)_{0.5}(OH)·0.11H_2O$ nanowires were hydrothermally grown on reduced graphene oxide, followed by thermal annealing at a relatively low temperature (ca. 350 ℃). The resulting CoP/RGO composite demonstrated excellent performance in anodes for lithium-ion batteries, delivering a specific capacity of 968 mA·h·g^{-1} at a current density of 0.2 A·g^{-1} during the 200th cycle, which was both higher and more stable than that shown by pure CoP nanowires (e.g., 431 mA·h·g^{-1} during the 100th cycle). CoP/RGO also exhibited superior rate performance (e.g., 424 mA·h·g^{-1} at a current density of 10 A·g^{-1}). Impressively, the cycling performance of the electrode was highly stable, showing a reversible specific capacity of 297 mA·h·g^{-1} at a current density of 20 A·g^{-1} during the 10,000th cycle. Its exceptional performance makes it a promising candidate for lithium storage applications.

2 Experimental

2.1 Preparation of graphene oxide (GO)

GO was synthesized from natural graphite powders using a modified version of Hummer's method [24, 25]. Graphite powder (1 g, Alfa Aesar), H_2SO_4 (92 mL, Alfa Aesar), and HNO_3 (24 mL, Alfa Aesar) were mixed and vigorously stirred in an ice bath. While stirring, $KMnO_4$ (6 g) (Sigma-Aldrich) was added slowly to the reaction solution. After stirring for 15 min, the temperature of the suspended solution was increased to 85 ℃, and maintained at that temperature for 1 h. After this time, distilled water (100 mL) was added dropwise to the solution, which was then kept at 85 ℃ for a further 30 min until a brilliant yellow suspension was obtained. Immediately after the reaction, H_2O_2 (35%, 10 mL) was added to the suspension to reduce the unreacted $KMnO_4$. The resulting suspension was centrifuged, and washed with HCl (10%) followed by distilled water until the pH value was close to 7. Finally, the GO was freeze-dried for later use. A GO suspension (5 mg·mL^{-1}) was prepared by dispersing the GO in deionized water.

2.2 Preparation of CoP nanowire/RGO composite

In a typical reaction, the GO suspension (5 mg·mL^{-1}, 8 mL), $CoCl_2·6H_2O$ (1.0 mmol), and urea (1.0 mmol) (Sigma-Aldrich) were added to 12 mL of deionized water and stirred for 10 min. The mixture was then transferred to a 23 mL Teflon-lined stainless steel autoclave. This was followed by autoclaving at 180 ℃ for 16 h. After cooling to room temperature, the deposits were washed with deionized water and dried at 50 ℃. Next, the Co precursor/RGO and NaH_2PO_2 (1.0 g) (Sigma-Aldrich) were placed in a porcelain boat at two separate positions, with NaH_2PO_2 at the upstream side of the furnace. The molar ratio of Co to P was 1:5. After flushing with Ar, the center of the furnace was elevated to 350 ℃ at a ramping rate of 3 ℃·min^{-1} and held at this temperature for 2 h, then naturally cooled to ambient temperature under an Ar atmosphere. The pure CoP nanowires were obtained by following a similar procedure as used for CoP/RGO, but without adding any GO suspension.

2.3 Characterization

The morphology of the samples was investigated using field-emission scanning electron microscopy (FESEM) (JEOL, Model JSM-7600F). Transmission electron microscopy (TEM) images were taken on a JEOL 2010F operating at 200 kV. The crystal structural characterization of the samples was carried out on a Shimadzu 6000 X-ray diffractometer at a scan rate of 2 °·min^{-1} with a 2θ range of 20° to 80° using a Cu Kα1 (λ = 0.15406 nm) radiation source. An accelerated surface area and porosimetry system (ASAP 3020) was used for the measurement of nitrogen adsorption/desorption isotherms at –196 °C. Before the measurement, all as-prepared samples were degassed for 8 h at 120 °C under vacuum. The specific surface areas were determined by the Brunauer–Emmett–Teller method (BET).

2.4 Electrochemical measurements

The working electrodes were fabricated by thoroughly mixing the samples with conductive carbon black and polyvinylidene fluoride (PVDF) as a binder in a weight ratio of 8:1:1, with N-methylpyrrolidone (NMP) acting as a solvent. The slurry was coated on copper foil and dried in a vacuum oven at 60 °C overnight. The electrochemical measurements were carried out at room temperature using two-electrode coin cells (X2 Labwares, Singapore) with pure lithium foil as both the counter and reference electrodes. A Celgard 2400 membrane was used as the separator, and the electrolyte was 1 M LiPF$_6$ in ethylene carbonate (EC)/diethyl carbonate (DEC) (1:1 in volume). Cell assembly was carried out in an Ar-filled glovebox with concentrations of moisture and oxygen below 1.0 ppm. All the cells were tested using an NEWARE multi-channel battery testing system with galvanostatic charge and discharge in a voltage range of 0.005–3.0 V. The electrode loading for each battery was 0.5 ± 0.1 mg·cm^{-2}, and the thickness of the electrode coating was 90 ± 10 μm.

3 Results and discussion

The CoP nanowire/RGO composites were prepared by a facile hydrothermal method using GO and CoCl$_2$ as the reactants, followed by an annealing process (Fig. 1).
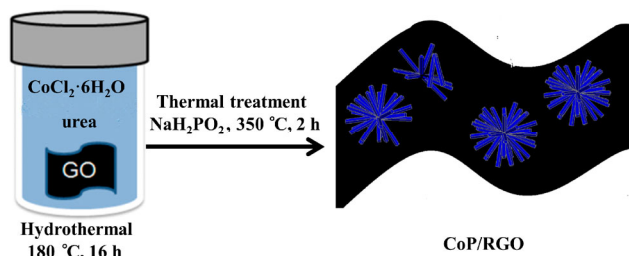
**Figure 1** Schematic of the synthesis of the CoP/RGO composite.

When NaH$_2$PO$_2$ was heated over 200 °C, the PH$_3$ generated could react with the Co precursor to form CoP. The diffraction peaks for the as-obtained precursor can be assigned to orthorhombic Co(CO$_3$)$_{0.5}$(OH)·0.11H$_2$O (JCPDS No. 48-0083) (see Fig. S1 in the Electronic Supplementary Material (ESM)). During the hydrothermal process, the GO was partially reduced into RGO due to thermal cleavage of the oxygen-containing groups [26, 27]. The pure RGO was also investigated, as shown in the SEM and TEM images (see Fig. S2 in the ESM). After the hydrothermal treatment, it assembled into a 3D porous structure.

The crystal structure of the CoP/RGO composite was characterized using X-ray diffraction (XRD). All the diffraction peaks can be assigned to orthorhombic CoP (JCPDS No. 29-0497) (Fig. 2(a)). To further confirm the existence of RGO in the composite, Raman spectroscopy was carried out. As shown in Fig. 2(b), there are two distinct bands located at 1,349 and 1,592 cm^{-1}, attributed to the D-band and G-band, respectively [28]. The D-band was caused by a disorder-induced phonon mode and the G-band by the E$_{2g}$ phonons of the sp^2-hybridized C atoms in graphene [29, 30]. Figure 2(c) shows a SEM image of the precursor, indicating that RGO sheets coated with CoP nanowires. After the phosphidation process, CoP nanowires grew uniformly on the surface of the RGO sheets (Fig. 2(d)), demonstrating the strong coupling effect between the CoP nanowires and RGO sheets [31–33]. In addition, the high-magnification SEM image (inset) shows that these nanowires were 200–300 nm in diameter and 10–20 μm in length.

The structure of the CoP/RGO was further investigated using TEM. In good agreement with the SEM images, the TEM images (Fig. 3(a) and Fig. S3 in the ESM) indicate that the diameter of CoP nanowires was around 250 nm. When examined more closely, the
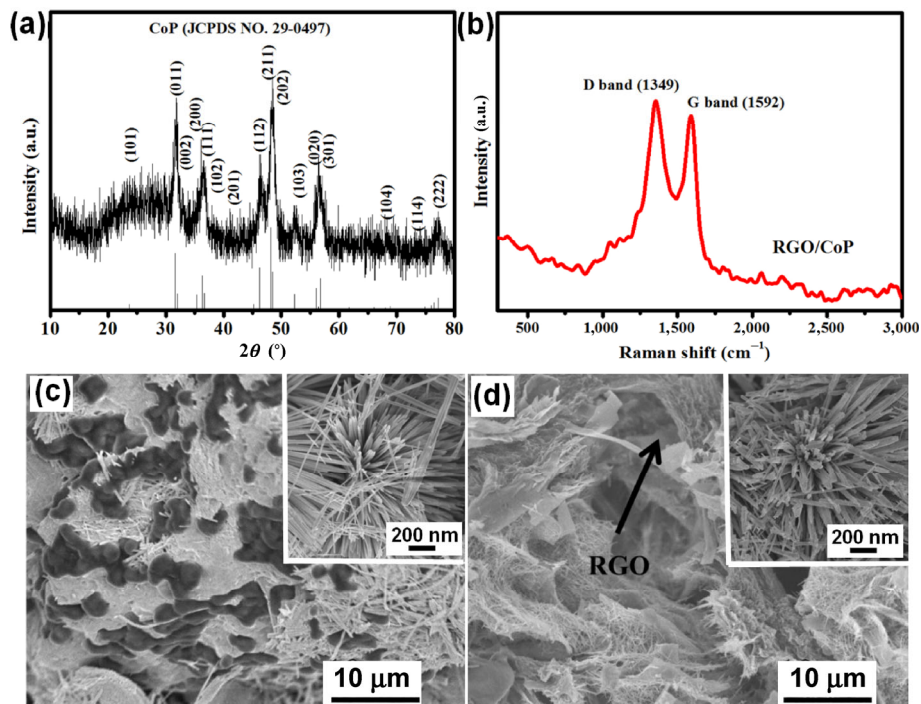
Figure 2 (a) XRD pattern of CoP/RGO, (b) Raman spectrum of CoP/RGO, (c) and (d) SEM images of Co precursor/RGO and the phosphidated sample, respectively, with insets showing high-magnification SEM images.
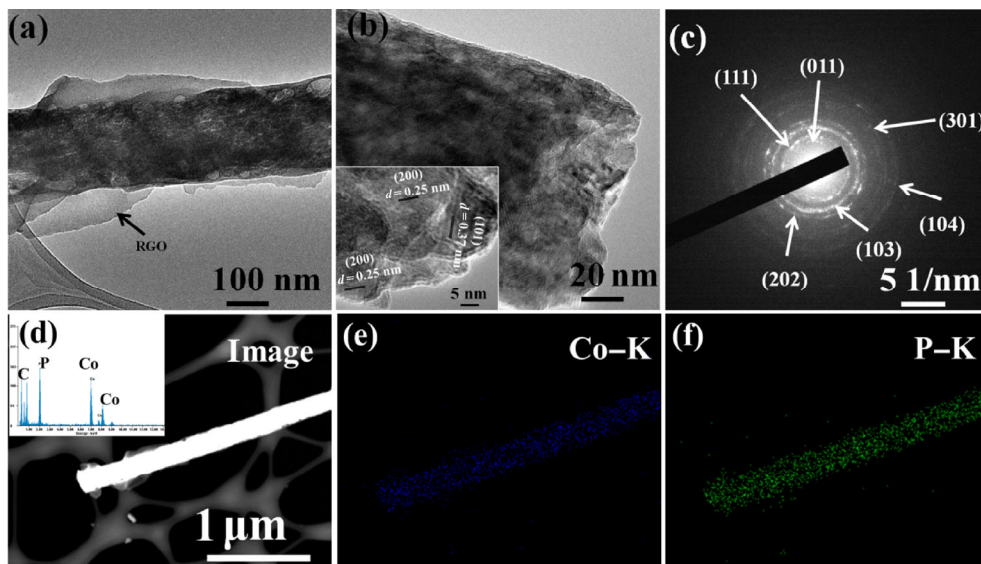
Figure 3 (a)–(c) TEM images and corresponding SAED patterns of CoP/RGO (inset of (b) shows a HRTEM image), (d) STEM image of CoP/RGO (inset shows the EDX spectrum), (e) and (f) elemental mapping images of P and Co for CoP/RGO.

porous structure of the CoP nanowires can be clearly observed (Fig. 3(b)). The inset of Fig. 3(b) shows a typical high-resolution TEM (HRTEM) image of CoP/RGO, in which well-resolved lattice fringes with interplanar distances of 0.37 and 0.25 nm can be indexed to the (101) and (200) planes of CoP, respectively. The diffraction rings in the selected area electron diffraction (SAED) pattern (Fig. 3(c)) are composed of discontinuous concentric rings that can be identified as the (011), (111), (202), (103), (301), and (104) planes of orthorhombic CoP, revealing that the nanowires are polycrystalline. The scanning TEM (STEM) image and the corresponding

energy dispersive X-ray spectroscopy (EDX) elemental mapping images of P and Co for CoP/RGO (Figs. 3(d)–3(f)) further indicate the presence of Co and P, with both elements being uniformly distributed in the nanowires. Nitrogen adsorption–desorption (see Fig. S3 in the ESM) was used to characterize the porous structure of CoP/RGO. The BET surface area of CoP/RGO was determined to be 29.1 $m^2 \cdot g^{-1}$, which was significantly higher than that of the CoP nanowires (15.9 $m^2 \cdot g^{-1}$), and the pore size distribution was in the 5–25 nm range, in agreement with the large pores observed in Fig. 3(b).

The CoP/RGO composite was tested as an anode material for lithium-ion batteries. Figures 4(a) and 4(b) show the cyclic voltammetry (CV) curves obtained between 0.005 and 3.0 V at a scan rate of 0.2 $mV \cdot s^{-1}$ and the galvanostatic discharge/charge profiles at a current density of 0.2 $A \cdot g^{-1}$, respectively. It can be seen that a cathodic peak appeared at ca. 1 V in the first cathodic sweep process (Fig. 4(a)), which corresponds to a voltage plateau in the first discharge profile

(Fig. 4(b)). This cathodic peak was related to the conversion reaction $CoP + 3Li^+ + 3e^- \rightarrow Co + Li_3P$. Additionally, a small peak at 0.6 V was observed, which was related to the reaction $CoP + Li^+ + e^- \rightarrow LiP + Co$ [19], and was accompanied by an irreversible reaction related to the decomposition of the organic electrolyte to form a solid electrolyte interphase (SEI) layer [34]. In the first anodic sweep process, one major and one minor peak appeared at 1.2 and 2.7 V, which can be attributed to the decomposition of the SEI layer and Li_3P ($Li_3P \rightarrow LiP + 2Li^+ + 2e^-$), respectively. During the subsequent cycles, the CV curves and the charge/discharge profiles were almost identical, indicating the reversible and stable electrochemical characteristics of the CoP/RGO composite. The CV curves of pure CoP showed similar peaks to those of CoP/RGO (see Fig. S4(a) in the ESM). As can be seen in Fig. 4(b), the CoP/RGO electrode delivered a discharge capacity of 2,057 $mA \cdot h \cdot g^{-1}$ and a charge capacity of 1,163 $mA \cdot h \cdot g^{-1}$, which was significantly higher than the theoretical specific capacity of CoP (894 $mA \cdot h \cdot g^{-1}$).
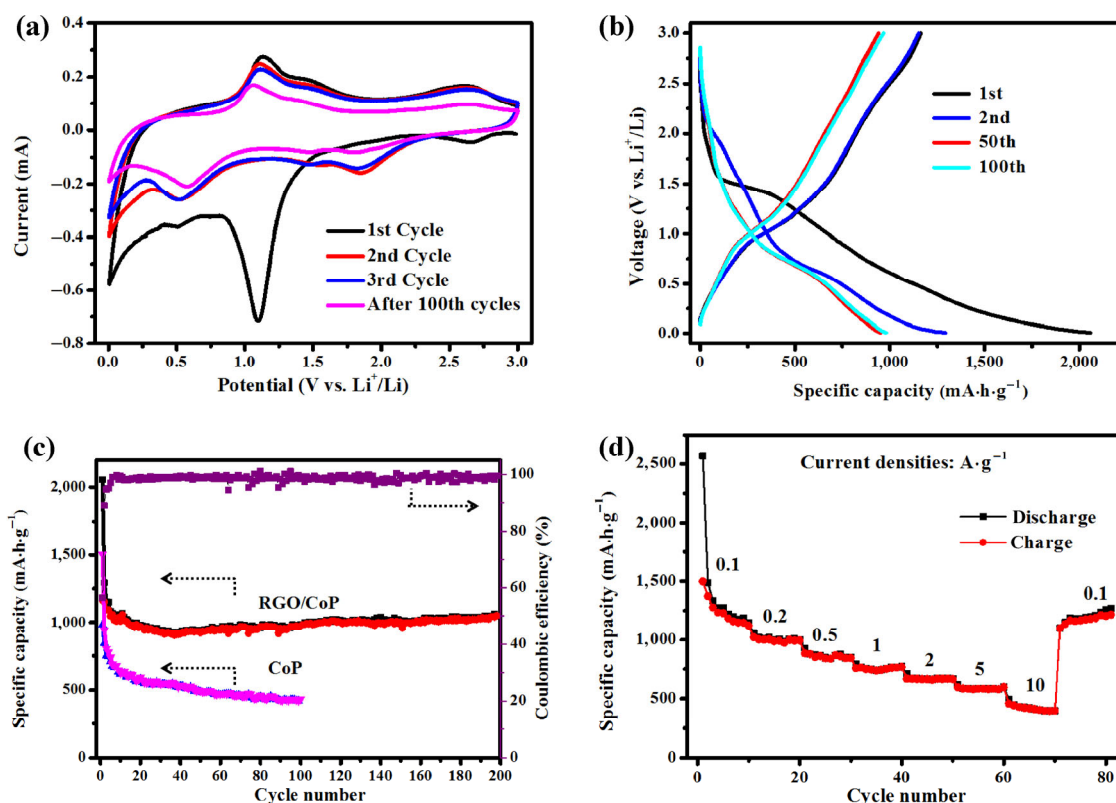

Figure 4 (a) Cyclic voltammograms of CoP/RGO between 0.005 and 3.0 V at a scan rate of 0.2 $mV \cdot s^{-1}$, (b) charge–discharge voltage profiles of CoP/RGO at a current density of 0.2 $A \cdot g^{-1}$, (c) cycling performances and Coulombic efficiencies of CoP/RGO and CoP at a current density of 0.2 $A \cdot g^{-1}$, and (d) comparison of charge and discharge capacities of CoP/RGO at various current rates.

The extra capacity was mainly a result of the formation of the SEI layer during the first discharge process [35–38]. All the potential plateaus observed in the discharge–charge curves are consistent with the redox peaks in the CV curves. During the second cycle, the CoP/RGO electrode delivered a discharge capacity of 1,292 mA·h·g^{-1} and a charge capacity of 1,152 mA·h·g^{-1}, corresponding to a Coulombic efficiency of 89.2%. Moreover, overlapping the 50th and 100th cycle discharge–charge curves shows the well-defined cyclability and reversibility of the conversion reactions as shown in Fig. 4(b).

The cycling performances and corresponding Coulombic efficiencies of the samples are shown in Fig. 4(c). It can be clearly seen that the CoP/RGO achieved a much higher capacity than the pure CoP. After 200 cycles at a current density of 200 mA·g^{-1}, a specific capacity of 967 mA·h·g^{-1} was retained for CoP/RGO, while the specific capacity of pure CoP nanowires rapidly decayed to 429 mA·h·g^{-1} after only 100 cycles. The thickness of the CoP/RGO electrode surface only increased slightly (Fig. S5 in the ESM). This could be due to the framework of CoP/RGO having a large amount of free space, allowing it to resist the fracturing caused by fluctuations in volume during the lithium insertion and removal reactions as shown in Fig. 4(b).

The charge–discharge rate capability was evaluated at current densities ranging from 0.1 to 10 A·g^{-1} (Fig. 4(d)). As can be seen, the specific capacities were 1,274, 998, 847, 741, 667, 586, and 424 mA·h·g^{-1} at current densities of 0.1, 0.2, 0.5, 1, 2, 5, and 10 A·g^{-1}, respectively. When the current density was reverted to 0.1 A·g^{-1} after 70 cycles, the initial reversible capacity returned to 1,183 mA·h·g^{-1}. This indicates that the porous CoP/RGO, with its large surface areas and good conductivity, enhanced the electrolyte/electrode contact area and improved charge transfer during the lithiation/de-lithiation processes, leading to a higher rate capability than was observed for CoP (see Fig. S4(b) in the ESM) [39–44].

Figure 5(a) shows the TEM image for the CoP/RGO anode in the lithiated state after the first discharge. Both the CoP/RGO embedded in the conducting carbon black and the nanowire structure can still be seen clearly, except for the SEI layer on the surface. According to the HRTEM result in Fig. 5(b), the dark areas can be indexed to metallic Co with a corresponding plane

1st discharged state (0.005 V)

1st recharged state (3 V)
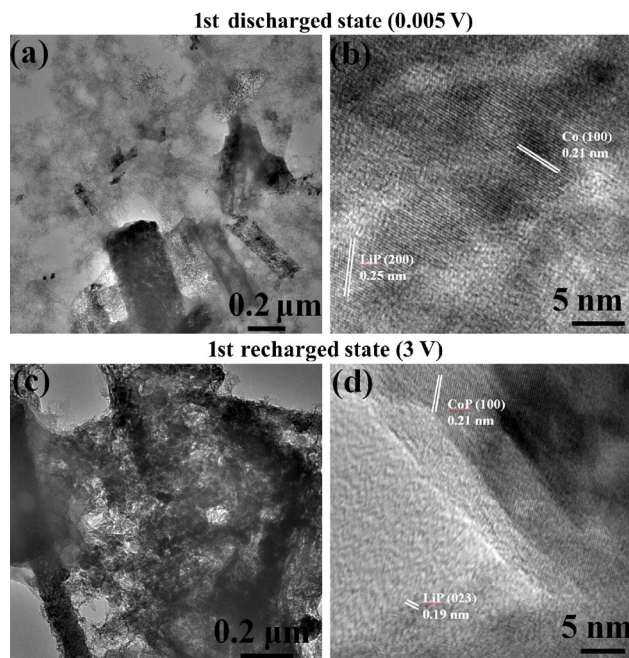
Figure 5 Microstructure of the CoP/RGO anode at the first cycle: (a) TEM image of the CoP/RGO anode in the lithiated state, (b) HRTEM image confirming the generation of LiP matrix and metallic Co, (c) TEM image of the CoP/RGO anode in the delithiated state (after the first recharge), and (d) HRTEM image confirming the regeneration of CoP nanocrystallines and remaining LiP.

of (100), while the bright background relates to the converted LiP matrix. The LiP phase is less visible than the Co phase due to the weak light scattering of the constituent elements. When the anode was recharged to 3.0 V, the TEM and HRTEM images (Figs. 5(c) and 5(d)) show the newly formed CoP instead of LiP and Co. However, a certain amount of LiP can still be seen in the bright background.

Fast discharge and/or charge rates and long cycling performances are favorable properties for practical applications. The CoP/RGO composite was charged/discharged at a current density of 20 A·g^{-1} (Fig. 6(a)). After continuous cycling for 10,000 cycles at this current density, it maintained a high specific capacity of 297 mA·h·g^{-1}. Gradually increasing reversible capacity during cycling has been observed for several previously reported electrode materials, and has been attributed to a gradual activation of the electrodes. Furthermore, the SEI layer built up on the surface as well as within the pores of the active material during the cycling process, which also contributed to the gradual increase in charge storage [45–47]. Moreover, the XRD pattern and TEM image in Fig. S6 in the ESM show that the

structure of the electrode materials was retained, with the diffraction peaks still matching the major peaks of CoP.

To understand the excellent Li storage performance of the CoP/RGO, electrochemical impedance spectroscopy (EIS) was carried, and the resulting Nyquist plots are shown in Fig. 6(b). Each Nyquist plot shows an intercept at a very high frequency related to the ohmic resistance (Re). The semicircles correspond to the charge-transfer impedance (R_{ct}) at medium frequencies, and a sloping line at low frequency is indexed to the Warburg impedance region (Wo). The CoP/RGO electrode showed a lower charge-transfer resistance (168 Ω) than the pure CoP electrode (264 Ω) before the charge/discharge cycling test. This suggests lower contact and charge-transfer impedances for the CoP/RGO electrode. The R_{ct} of the composite increased slightly after prolonged cycling (to 174 Ω after 100 cycles), which was still lower than that observed for the

pure CoP electrode (283 Ω after 100 cycles). Moreover, the CoP/RGO sample exhibited a steeper gradient at low frequency, indicating a more rapid lithium-ion diffusion process in CoP/RGO than in pure CoP. This could be related to the advantageous structural features of the CoP/RGO allowing the retention of the structural integrity of the electrode and improved kinetics during lithium insertion and removal [48].

Figure 7 shows the XRD patterns and SEM images of the CoP/RGO electrode after being charged/discharged for 100 cycles at a current density of 0.2 A·g^{-1}. In Fig. 7(a), the SEM image shows that the morphology and structure of the electrode materials were well maintained, except for some agglomeration caused by the redox reactions during the charge–discharge processes. In addition, the XRD peaks still match the major peaks of CoP (Fig. 7(b)). This also indicates the reversible electrochemical characteristics of the composite.
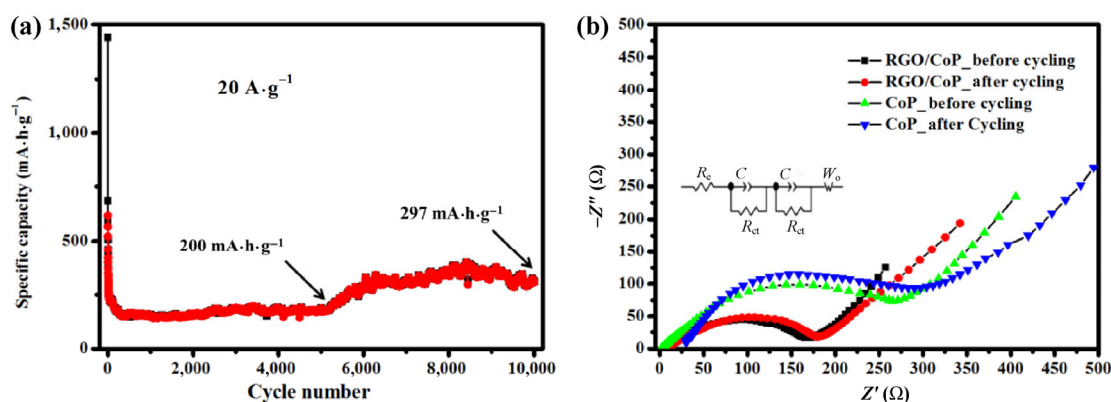
Figure 6 (a) Cycling performance of CoP/RGO at a current density of 20 A·g^{-1}. (b) Nyquist plots of CoP/RGO and CoP before and after cycling. CPE is the constant phase angle element, which was used to replace the capacitance for convenience of fitting.
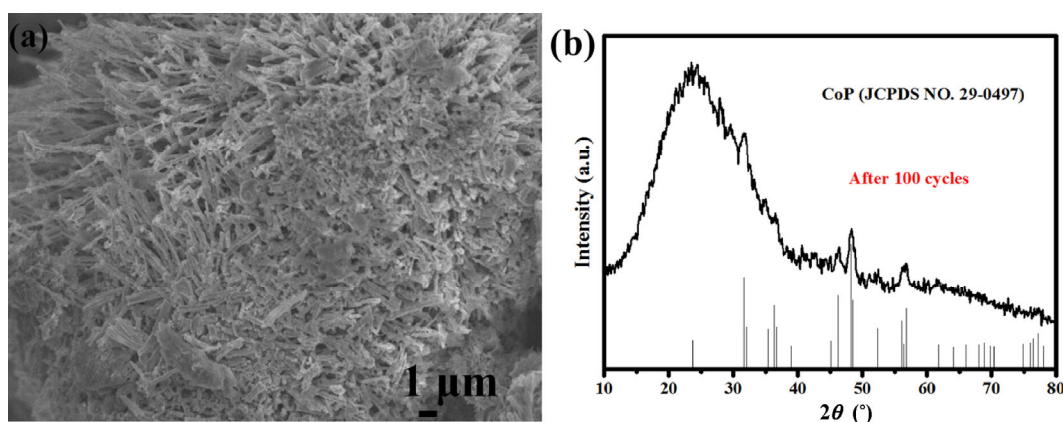
Figure 7 (a) SEM image and (b) XRD pattern of CoP/RGO after discharging–charging for 100 cycles at a current density of 0.2 A·g^{-1}.

4 Conclusions

In summary, we developed a facile approach to allow the direct growth of CoP nanowires on the surface of RGO to yield an anode material for lithium-ion batteries. The conductivity of the composite was greatly enhanced in comparison to pure CoP, which is useful for the rapid transport of ions and electrons. The CoP/RGO nano-composite demonstrated a highly reversible lithium storage capacity of 967 mA·h·g^{-1} over 200 cycles at a current density of 0.2 A·g^{-1}, and an excellent charge–discharge rate performance (e.g., 424 mA·h·g^{-1} at a current density of 10 A·g^{-1}), which makes it attractive as an anode material for high performance lithium-ion batteries.

Acknowledgements

Electronic Supplementary Material: Supplementary material (TEM measurements, N_2 adsorption–desorption isotherms measurements, and surface thickness measurement, etc.) is available in the online version of this article at http://dx.doi.org/10.1007/s12274-015-0941-5.

References

[1] Dunn, B.; Kamath, H.; Tarascon, J. M. Electrical energy storage for the grid: A battery of choices. *Science* **2011**, *334*, 928–935.

[2] Goodenough, J. B.; Park, K. S. The Li-ion rechargeable battery: A perspective. *J. Am. Chem. Soc.* **2013**, *135*, 1167–1176.

[3] Wang, H. J.; Dai, H. J. Strongly coupled inorganic–nano-carbon hybrid materials for energy storage. *Chem. Soc. Rev.* **2013**, *42*, 3088–3113.

[4] Simon, P.; Gogotsi, Y. Materials for electrochemical capacitors. *Nat. Mater.* **2008**, *7*, 845–854.

[5] Yao, Y.; McDowell, M. T.; Ryu, I.; Wu, H.; Liu, N.; Hu, L. B.; Nix, W. D.; Cui, Y. Interconnected silicon hollow nanospheres for lithium-ion battery anodes with long cycle life. *Nano Lett.* **2011**, *11*, 2949–2954.

[6] Yuan, C. Z.; Wu, H. B.; Xie, Y.; Lou, X. W. Mixed transition-metal oxides: Design, synthesis, and energy-related applications. *Angew. Chem., Int. Ed.* **2014**, *53*, 1488–1504.

[7] Reddy, M. V.; Rao, G. V. S.; Chowdari, B. V. R. Metal oxides and oxysalts as anode materials for Li ion batteries. *Chem. Rev.* **2013**, *113*, 5364–5457.

[8] Liu, J.; Xia, H.; Xue, D. F.; Lu, L. Double-shelled nano-capsules of V_2O_5-based composites as high-performance anode and cathode materials for Li ion batteries. *J. Am. Chem. Soc.* **2009**, *131*, 12086–12087.

[9] Reddy, A. L. M.; Shaijumon, M. M.; Gowda, S. R.; Ajayan, P. M. Coaxial MnO_2/carbon nanotube array electrodes for high-performance lithium batteries. *Nano Lett.* **2009**, *9*, 1002–1006.

[10] Cabana, J.; Monconduit, L.; Larcher, D.; Palacín, M. R. Beyond intercalation-based Li-ion batteries: The state of the art and challenges of electrode materials reacting through conversion reactions. *Adv. Mater.* **2010**, *22*, 170–192.

[11] Popczun, E. J.; McKone, J. R.; Read, C. G.; Biacchi, A. J.; Wiltrout, A. M.; Lewis, N. S.; Schaak, R. E. Nanostructured nickel phosphide as an electrocatalyst for the hydrogen evolution reaction. *J. Am. Chem. Soc.* **2013**, *135*, 9267–9270.

[12] Jiang, P.; Liu, Q.; Sun, X. P. NiP_2 nanosheet arrays supported on carbon cloth: An efficient 3D hydrogen evolution cathode in both acidic and alkaline solutions. *Nanoscale* **2014**, *6*, 13440–13445.

[13] Callejas, J. F.; McEnaney, J. M.; Read, C. G.; Crompton, J. C.; Biacchi, A. J.; Popczun, E. J.; Gordon, T. R.; Lewis, N. S.; Schaak R. E. Electrocatalytic and photocatalytic hydrogen production from acidic and neutral-pH aqueous solutions using iron phosphide nanoparticles. *ACS Nano* **2014**, *8*, 11101–11107.

[14] Tian, J. Q.; Liu, Q.; Liang, Y. H.; Xing, Z. C.; Asiri, A. M.; Sun, X. P. FeP nanoparticles film grown on carbon cloth: An ultrahighly active 3D hydrogen evolution cathode in both acidic and neutral solutions. *ACS Appl. Mater. Interfaces* **2014**, *6*, 20579–20584.

[15] Tian, J. Q.; Cheng, N. Y.; Liu, Q.; Xing, W.; Sun, X. P. Cobalt phosphide nanowires: Efficient nanostructures for fluorescence sensing of biomolecules and photocatalytic evolution of dihydrogen from water under visible light. *Angew. Chem., Int. Ed.* **2015**, *54*, 5493–5497.

[16] Yang, D.; Zhu, J. X.; Rui, X. H.; Tan, H. T.; Cai, R.; Hoster, H. E.; Yu, D. Y. W.; Hng, H. H.; Yan, Q. Y. Synthesis of cobalt phosphides and their application as anodes for lithium ion batteries. *ACS Appl. Mater. Interfaces* **2013**, *5*, 1093–1099.

[17] Tian, J. Q.; Liu, Q.; Cheng, N. Y.; Asiri, A. M.; Sun, X. P. Self-supported Cu_3P nanowire arrays as an integrated high-performance three-dimensional cathode for generating hydrogen from water. *Angew. Chem., Int. Ed.* **2014**, *53*, 9577–9581.

[18] Xing, Z. C.; Liu, Q.; Asiri, A. M.; Sun, X. P. Closely interconnected network of molybdenum phosphide nano-particles: A highly efficient electrocatalyst for generating hydrogen from water. *Adv. Mater.* **2014**, *26*, 5702–5707.

[19] Zhang, Z. S.; Yang, J.; Nuli, Y.; Wang, B. F.; Xu, J. Q. CoP_x synthesis and lithiation by ball-milling for anode materials of lithium ion cells. *Solid State Ionics* **2005**, *176*, 693–697.

[20] Yang, Z. H.; Liu, L.; Wang, X. Y.; Yang, S. Y.; Su, X. P. Stability and electronic structure of the Co–P compounds from first-principle calculations. *J. Alloys Compd.* **2011**, *509*, 165–171.

[21] Yang, D. S.; Bhattacharjya, D.; Inamdar, S.; Park, J.; Yu, J. S. Phosphorus-doped ordered mesoporous carbons with different lengths as efficient metal-free electrocatalysts for oxygen reduction reaction in alkaline media. *J. Am. Chem. Soc.* **2012**, *134*, 16127–16130.

[22] Oyama, S. T.; Gott, T.; Zhao, H. Y.; Lee, Y.-K. Transition metal phosphide hydroprocessing catalysts: A review. *Catal. Today* **2009**, *143*, 94–107.

[23] Xia, X. H.; Chao, D. L.; Zhang, Y. Q.; Shen, Z. X.; Fan, H. J. Three-dimensional graphene and their integrated electrodes. *Nano Today* **2014**, *9*, 785–807.

[24] Hummers, W. S. Jr.; Offeman, R. E. Preparation of graphitic oxide. *J. Am. Chem. Soc.* **1958**, *80*, 1339.

[25] Geng, J. X.; Jung, H. T. Porphyrin functionalized graphene sheets in aqueous suspensions: From the preparation of graphene sheets to highly conductive graphene films. *J. Phys. Chem. C* **2010**, *114*, 8227–8234.

[26] Wang, B.; Zhu, T.; Wu, H. B.; Xu, R.; Chen, J. S.; Lou, X. W. Porous Co_3O_4 nanowires derived from long $Co(CO_3)_{0.5}(OH)\cdot0.11H_2O$ nanowires with improved supercapacitive properties. *Nanoscale* **2012**, *4*, 2145–2149.

[27] Gong, Y. J.; Yang, S. B.; Zhan, L.; Ma, L. L.; Vajtai, R.; Ajayan, P. M. A bottom-up approach to build 3D architectures from nanosheets for superior lithium storage. *Adv. Funct. Mater.* **2014**, *24*, 125–130.

[28] Shi, Y.; Wang, J. Z.; Chou, S. L.; Wexler, D.; Li, H. J.; Ozawa, K.; Liu, H. K.; Wu, Y. P. Hollow structured Li_3VO_4 wrapped with graphene nanosheets *in situ* prepared by a one-pot template-free method as an anode for lithium-ion batteries. *Nano Lett.* **2013**, *13*, 4715–4720.

[29] Wu, X. L.; Jiang, L. Y.; Cao, F. F.; Guo, Y. G.; Wan, L. J. $LiFePO_4$ nanoparticles embedded in a nanoporous carbon matrix: Superior cathode material for electrochemical energy-storage devices. *Adv. Mater.* **2009**, *21*, 2710–2714.

[30] Li, Y. Z.; Zhou, Z.; Gao, X. P.; Yan, J. A novel sol-gel method to synthesize nanocrystalline $LiVPO_4F$ and its electrochemical Li intercalation performances. *J. Power Sources* **2006**, *160*, 633–637.

[31] Zhou, X. S.; Wan, L. J.; Guo, Y. G. Binding SnO_2 nano-crystals in nitrogen-doped graphene sheets as anode materials for lithium-ion batteries. *Adv. Mater.* **2013**, *25*, 2152–2157.

[32] Zhou, G. M.; Wang, D. W.; Yin, L. C.; Li, N.; Li, F.; Cheng, H. M. Oxygen bridges between NiO nanosheets and graphene for improvement of lithium storage. *ACS Nano* **2012**, *6*, 3214–3223.

[33] Liang, Y. Y.; Wang, H. L.; Zhou, J. G.; Li, Y. G.; Wang, J.; Regier, T.; Dai, H. J. Covalent hybrid of spinel manganese–cobalt oxide and graphene as advanced oxygen reduction electrocatalysts. *J. Am. Chem. Soc.* **2012**, *134*, 3517–3523.

[34] López, M. C.; Ortiz, G. F.; Tirado, J. L. A functionalized Co_2P negative electrode for batteries demanding high Li-potential reaction. *J. Electrochem. Soc.* **2012**, *159*, A1253–A1261.

[35] Lu, Y.; Tu, J. P.; Xiang, J. Y.; Wang, X. L.; Zhang, J.; Mai, Y. J.; Mao, S. X. Improved electrochemical performance of self-assembled hierarchical nanostructured nickel phosphide as a negative electrode for lithium ion batteries. *J. Phys. Chem. C* **2011**, *115*, 23760–23767.

[36] Lu, Y.; Tu, J. P.; Xiong, Q. Q.; Qiao, Y. Q.; Wang, X. L.; Gu, C. D.; Mao, S. X. Synthesis of dinickel phosphide (Ni_2P) for fast lithium-ion transportation: A new class of nanowires with exceptionally improved electrochemical performance as a negative electrode. *RSC Adv.* **2012**, *2*, 3430–3436.

[37] Carenco, S.; Surcin, C.; Morcrette, M.; Larcher, D.; Mézailles, N.; Boissière, C.; Sanchez, C. Improving the Li-electrochemical properties of monodisperse Ni_2P nanoparticles by self-generated carbon coating. *Chem. Mater.* **2012**, *24*, 688–697.

[38] Boyanov, S.; Zitoun, D.; Ménétrier, M.; Jumas, J. C.; Womes, M.; Monconduit, L. Comparison of the electrochemical lithiation/delitiation mechanisms of FeP_x (x = 1, 2, 4) based electrodes in Li-ion batteries. *J. Phys. Chem. C* **2009**, *113*, 21441–21452.

[39] Zhou, J.; Tian, G. H.; Chen, Y. J.; Meng, X. Y.; Shi, Y. H.; Cao, X. R.; Pan, K.; Fu, H. G. *In situ* controlled growth of $ZnIn_2S_4$ nanosheets on reduced graphene oxide for enhanced photocatalytic hydrogen production performance. *Chem. Commun.* **2013**, *49*, 2237–2239.

[40] Liu, J. H.; Liu, X. W. Two-dimensional nanoarchitectures for lithium storage. *Adv. Mater.* **2012**, *24*, 4097–4111.

[41] Xu, C. H.; Xu, B. H.; Gu, Y.; Xiong, Z. G.; Sun, J.; Zhao, X. S. Graphene-based electrodes for electrochemical energy storage. *Energy Environ. Sci.* **2013**, *6*, 1388–1414.

[42] Han, S.; Wu, D. Q.; Li, S.; Zhang, F.; Feng, X. L. Graphene: A two-dimensional platform for lithium storage. *Small* **2013**, *9*, 1173–1187.

[43] Liu, R.; Duay, J.; Lee, S. B. Heterogeneous nanostructured electrode materials for electrochemical energy storage. *Chem. Commun.* **2011**, *47*, 1384–1404.

[44] Wu, C. Z.; Yin, P.; Zhu, X.; Ouyang, C. Z.; Xie, Y. Synthesis of hematite (α-Fe$_2$O$_3$) nanorods: Diameter-size and shape effects on their applications in magnetism, lithium ion battery, and gas sensors. *J. Phys. Chem. B* **2006**, *110*, 17806–17812.

[45] Sun, Y. M.; Hu, X. L.; Luo, W.; Xia, F. F.; Huang, Y. H. Reconstruction of conformal nanoscale MnO on graphene as a high-capacity and long-life anode material for lithium ion batteries. *Adv. Funct. Mater.* **2013**, *23*, 2436–2444.

[46] Peng, C. X.; Chen, B. D.; Qin, Y.; Yang, S. H.; Li, C. Z.; Zuo, Y. H.; Liu, S. Y.; Yang, J. H. Facile ultrasonic synthesis of CoO quantum dot/graphene nanosheet composites with high lithium storage capacity. *ACS Nano* **2012**, *6*, 1074–1081.

[47] Luo, W.; Hu, X. L.; Sun, Y. M.; Huang, Y. H. Electrospun porous ZnCo$_2$O$_4$ nanotubes as a high-performance anode material for lithium-ion batteries. *J. Mater. Chem.* **2012**, *22*, 8916–8921.

[48] Wang, L.; Dong, Z. H.; Wang, Z. G.; Zhang, F. X.; Jin, J. Layered α-Co(OH)$_2$ nanocones as electrode materials for pseudocapacitors: Understanding the effect of interlayer space on electrochemical activity. *Adv. Funct. Mater.* **2013**, *23*, 2758–2764.